implies that the pairing potential is strongest in very underdoped samples. This finding may place strong constraints on theories of the pairing mechanism. The trend [opposite to that of the superfluid density n_s (20, 21), which decreases as x decreases] implies a scenario for underdoped cuprates that is radically different from that inferred from n_s and T_{c0} alone. The physical picture is that, in hole-doped cuprates, the pairing potential Δ_0 is maximal in the underdoped regime and falls rapidly with increased hole density, as anticipated in early resonating-valence-bond theories (15, 16). However, the small n_s at small x renders the condensate highly susceptible to phase fluctuations (17). At T_{c0}, spontaneous nucleation of highly mobile vortices destroys long-range phase coherence and the Meissner state (7, 22, 23), but vortex excitations remain observable to much higher T (5, 6). As x is increased, n_s and T_{c0} initially increase, but beyond $x = 0.17$, T_{c0} is suppressed by a steeply falling Δ_0. The trade-off between n_s and Δ_0 informs the entire cuprate phase diagram and accounts naturally for the dome shape of the curve of T_{c0} versus x.

An interesting implication may be inferred in the limit of small x. If the trend in ξ_0 in Fig. 4B persists, ξ_0 becomes smaller than the separation d of Cooper pairs in this limit ($d \sim 25$ Å at $x = 0.05$). For $x < 0.05$, we may treat the carriers as tightly bound pairs (bosons) that are well separated and too dilute to sustain long-range phase coherence. In uncovering the increased pairing strength at small x, our experiment provides clues that bosonic pairs may exist in this limit.

References and Notes

1. M. Tinkham, *Introduction to Superconductivity* (McGraw-Hill, New York, ed. 2, 1996).
2. H. Ding et al., *Phys. Rev. Lett.* **87**, 227001 (2001).
3. S. H. Pan et al., *Phys. Rev. Lett.* **85**, 1536 (2000).
4. J. E. Hoffman et al., *Science* **295**, 466 (2002).
5. Z. A. Xu, N. P. Ong, Y. Wang, T. Kakeshita, S. Uchida, *Nature* **406**, 486 (2000).
6. Y. Wang et al., *Phys. Rev. B* **64**, 224519 (2001).
7. Y. Wang et al., *Phys. Rev. Lett.* **88**, 257003 (2002).
8. F. Vidal, *Phys. Rev. B* **8**, 1982 (1973).
9. C. Capan et al., *Phys. Rev. Lett.* **88**, 56601 (2002).
10. P. Fournier et al., *Phys. Rev. B* **56**, 14149 (1997).
11. F. Gollnik, M. Naito, *Phys. Rev. B* **58**, 11734 (1998).
12. A. P. Mackenzie et al., *Phys. Rev. Lett.* **71**, 1238 (1993).
13. M. S. Osofsky et al., *Phys. Rev. Lett.* **71**, 2315 (1993).
14. Y. Ando et al., *Phys. Rev. B* **60**, 12475 (1999).
15. G. Baskaran, Z. Zou, P. W. Anderson, *Solid State Commun.* **63**, 973 (1987).
16. G. Kotliar, J. Liu, *Phys. Rev. B* **38**, 5142 (1988).
17. V. J. Emery, S. A. Kivelson, *Nature* **374**, 434 (1995).
18. Materials and methods are available as supporting material on *Science* Online.
19. T. Shibauchi, L. Krusin-Elbaum, Ming Li, M. P. Maley, P. H. Kes, *Phys. Rev. Lett.* **86**, 5763 (2001).
20. D. A. Bonn et al., *Czech J. Phys.* **46**, 3195 (1996).
21. Y. J. Uemura et al., *Phys. Rev. Lett.* **62**, 2317 (1989).
22. Z. Tešanović, *Phys. Rev. B* **51**, 16204 (1995).
23. A. K. Nguyen, A. Sudbø, *Phys. Rev. B* **57**, 3123 (1998).
24. We thank S. Hannahs for help with measurements at the National High Magnetic Field Laboratory, Tallahassee, FL, a facility supported by NSF and the

Three-Dimensional Mapping of Dislocation Avalanches: Clustering and Space/Time Coupling

Jérôme Weiss[1] and David Marsan[2]

There is growing evidence for the complex, intermittent, and heterogeneous character of plastic flow. Here we report a three-dimensional mapping of dislocation avalanches during creep deformation of an ice crystal, from a multiple-transducers acoustic emission analysis. Correlation analysis shows that dislocation avalanches are spatially clustered according to a fractal pattern and that the closer in time two avalanches are, the larger the probability is that they will be closer in space. Such a space/time coupling may contribute to the self-organization of the avalanches into a clustered pattern.

Dislocation-driven plastic deformation has been described as a smooth flow process that is homogeneous in both space and time, yet there is evidence for the intermittent and heterogeneous character of plastic flow (1). The spontaneous formation of fractal dislocation cell patterns has been reported in metals (2, 3), and scale-invariant patterning of dislocation arrays was also obtained in numerical simulations (4). These observations, however, provide a static characterization of the spatial heterogeneity of dislocation patterns after deformation. Surface observations in metals indicate that slip consists of intermittent events localized along slip bands (1), and the temporal heterogeneity of slip has been extensively explored in the Portevin-Le Chatelier effect (5). Recently, acoustic emission (AE) studies performed during the creep of single ice crystals, coupled with numerical simulations of collective dislocation motion, revealed a strongly intermittent plastic flow characterized by jerks of dislocations with power law distributions of energies $P(E) \sim E^{-\tau}$ (6–8) where $P(E)$ is the probability density function of the energy E. This feature is shared by other slowly driven systems (9), including fracture in disordered materials (10, 11). These dislocation avalanches are also clustered in time (12). In these experiments, complexity and multiscale properties arose solely from dislocations interacting via long-range internal stresses (decreasing with the distance r as $1/r$).

The evidence for heterogeneity and scale invariance in space, time, and energy calls for the development of new models of dislocation systems and plastic flow (13) and for a nonequilibrium statistical theory of dislocation motion (7). Yet, to further constrain theoretical development, a complete dynamical picture of plastic flow simultaneously in space, time, and energy domains is still lacking. Here we present three-dimensional (3D) mapping of dislocation avalanches during viscoplastic deformation of a crystalline material. The experiment, performed on a single crystal of ice Ih, was similar to those performed previously (7, 12), except that we used multiple transducers to map the hypocenters of the microseismic waves generated by the sudden local displacements associated with the dislocation avalanches. Compression creep (constant load) was applied to a cylindrical crystal under stress and temperature conditions in which diffusional creep is not a significant mechanism of inelastic deformation. Ice is an ideal material in which to explore collective dislocation dynamics with AE measurements: It deforms by dislocation slip even at temperatures close to the melting point; its transparency allows microcracking to be ruled out as a source of AE; and the transducers can be frozen on the specimen, yielding optimum acoustic coupling (6, 7, 14). The basal planes, which are the preferred slip planes in hexagonal ice, were inclined at the beginning of the test to 11° from the compression axis. A classical macroscopic creep behavior was observed, with primary and secondary creep followed by a roughly exponential growth of the strain rate during tertiary creep. Here, tertiary creep did not result from microcracking but from a rapid multiplication of dislocations. Because acoustic activity is a proxy of global deformation (14), most of the

[1]Laboratoire de Glaciologie et Géophysique de l'Environnement–CNRS, 54 rue Molière, BP 96, 38402 St. Martin d'Hères Cedex, France. [2]Laboratoire de Géophysique Interne et Tectonophysique, Université de Savoie, 73376 Le Bourget du Lac Cedex, France.
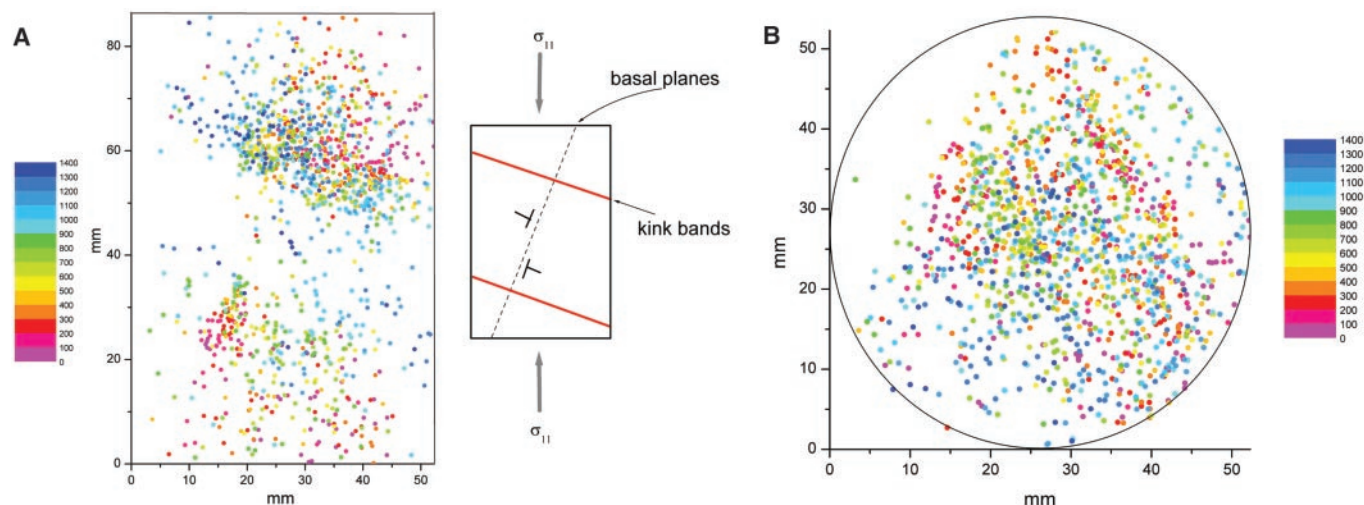
Fig. 1. 3D mapping of dislocation avalanches during creep of an ice crystal: (**A**) vertical and (**B**) horizontal projection of the hypocenters. A uniaxial compressive stress σ_{11} of 1.1 MPa was applied to the cylindrical sample (length = 86.5 mm, diameter = 52.3 mm), which led to a resolved shear stress on the basal planes of 0.21 MPa. The temperature was −10°C. Hypocenter locations were obtained from the arrival times at five acoustic transducers, using a constant wave velocity of 3950 ms^{-1}. The frequency bandwidth of the transducers was 0.1 to 1 MHz, and the amplitude range between the minimum and maximum recordable thresholds was 50 dB. The hypocenters, which are concentrated on the vertical projection along two bands perpendicular to the slip planes, have been colored as a function of their occurrence rank within the sequence of events. This reveals a migration of the avalanches, because the first events are preferentially located in the upper right and lower left corners and the last ones are in the upper left and lower right corners of the vertical projection.

acoustic events were recorded during this tertiary creep. In agreement with previous results (7), a power law distribution of energies was observed over more than five orders of magnitude, with an exponent $\tau = 1.6$. The plastic anisotropy of ice, coupled with the applied boundary conditions and the inclination of the basal planes, induced bending moments. In polycrystalline ice, such bending moments are relieved by lattice curvature, followed by the formation of subboundaries and kink bands, which consist of dislocations grouped in walls perpendicular to the basal planes, and by a rotation of the basal planes toward the compression axis (15). This mechanism, called continuous recrystallization, leads to the formation of new grains. A similar mechanism was observed during our experiment, with a rotation of the basal planes from 11° to 4° from the compression axis, and with the nucleation of two new grains at both ends of the sample at the end of the test. As expected, the grain boundaries were perpendicular to the initial basal orientation.

The location of the AE sources was computed from the arrival times of a wave at five transducers, in a way similar to that employed to locate microcracking events in rocks (16, 17). The time resolution of the recording device was 0.1 μs, leading to a lower bound for the spatial resolution of 400 μm. Only the dislocation avalanches that were detected by the five stations were located; that is, essentially the largest ones. This filtering happened homogeneously in time and in space. A vertical and a horizontal projection of the located hypocenters show (Fig. 1) (i) a clustering of dislocation avalanches on the vertical projection along a direction perpendicular to the slip (basal) planes, in agreement with

Fig. 2. Correlation integral analysis of the hypocenter locations (circles). $C(r)$, which is the probability of two locations being separated by less than r, scales as $C(r) \sim r^D$, with a correlation dimension $D = 2.5 \pm 0.1$ (circles) over about 1.5 orders of magnitude. A similar analysis was also performed for the same number of locations randomly distributed (a Poisson distribution) within the cylinder (crosses), which gives $D = 2.9 \pm 0.1$, which is in agreement with the theoretical expected value of 3. This demonstrates that the clustering of dislocation avalanches revealed by the correlation analysis is not affected by the size or the shape of the sample. Scaling analysis is limited toward small scales by the resolution threshold that induces an identical localization for several hypocenters, and therefore an artificial clustering, whereas a finite size effect is visible toward large scale.
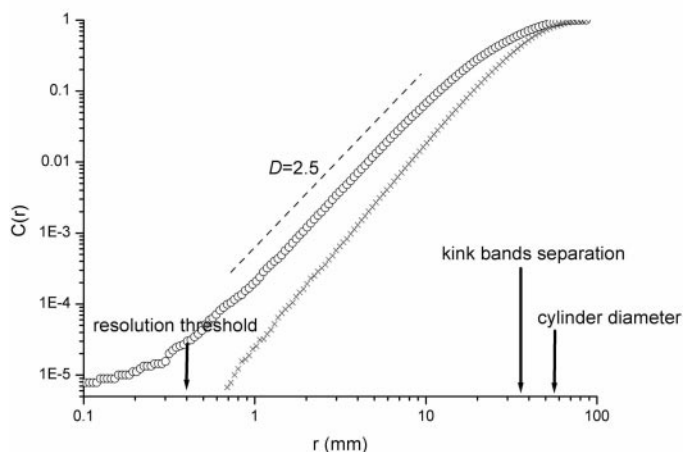
the formation of kink bands, which will eventually organize into new boundaries; (ii) a migration of the avalanches along this direction, characterized by a pointlike symmetry around the center as the crystal creeps; and (iii) a possible preferential alignment of the avalanches on the horizontal projection, especially for the first 300 events (red dots in Fig. 1). The migration of the AE hypocenters [observation (ii)] might be related to the crystal rotation and the buildup of kink bands. An analysis of the 3D spatial organization of the dislocation avalanches was performed by means of a correlation integral analysis (Fig. 2). Within a scale range limited toward small scale by the spatial resolution threshold

and toward large scale by a finite size effect (sample diameter = 52.3 mm), we observed a scale-invariant spatial distribution of avalanche locations with a correlation dimension $D = 2.5 \pm 0.1$. Whereas observations (i) and (ii) listed above are linked to the bending moments induced by the boundary conditions, this scale-invariant emerging structure results from the collective dislocation dynamics that self-organize into a scale-free clustered pattern of avalanches. This picture completes the static observations of scale-invariant dislocation structures (2, 3) as well as the scaling properties in terms of dissipated energy (7). This suggests a dislocation system in a close-to-critical state within a mate-
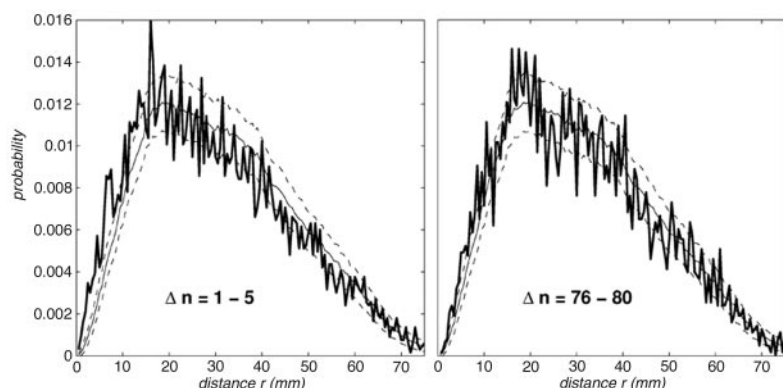
Fig. 3. Space/time coupling in the dislocation dynamics. Probabilities $P_{\Delta n}(r)$ (thick solid line) and $P(r)$ (thin solid line) for Δn ranging between 1 and 5 (left) and 76 and 80 (right), along with the error envelope (dashed lines) giving the standard deviation of the fluctuations around $P(r)$ that can occur by chance. A significant departure of $P_{\Delta n}(r)$ from $P(r)$ (that is, favored triggering of avalanches) is observed at distances up to about 20 mm (an important proportion of the sampled volume) for both Δn windows. These graphs in log-log scale are available as supporting material on *Science* Online.
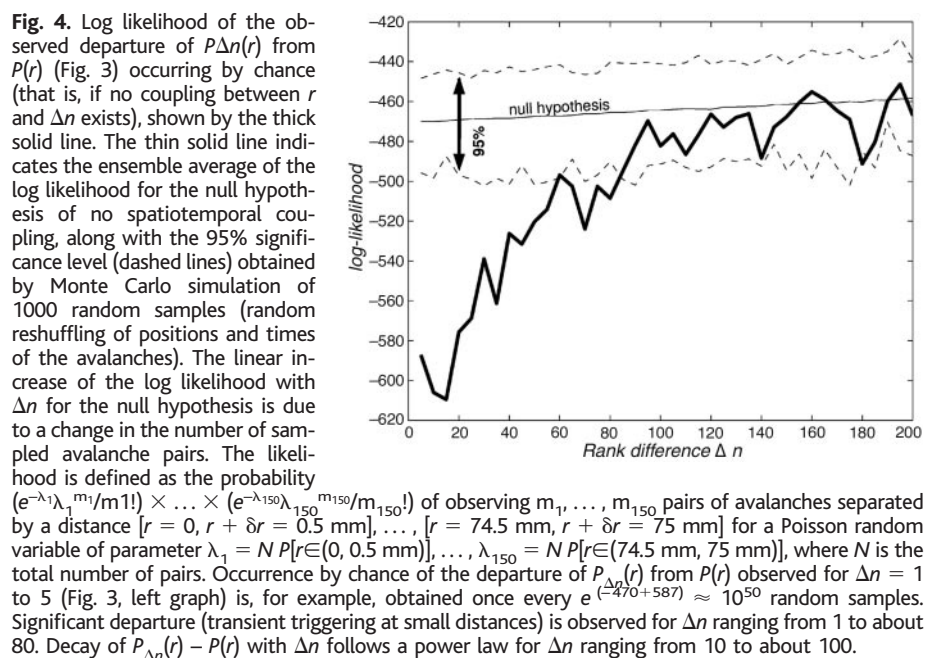
Fig. 4. Log likelihood of the observed departure of $P\Delta n(r)$ from $P(r)$ (Fig. 3) occurring by chance (that is, if no coupling between r and Δn exists), shown by the thick solid line. The thin solid line indicates the ensemble average of the log likelihood for the null hypothesis of no spatiotemporal coupling, along with the 95% significance level (dashed lines) obtained by Monte Carlo simulation of 1000 random samples (random reshuffling of positions and times of the avalanches). The linear increase of the log likelihood with Δn for the null hypothesis is due to a change in the number of sampled avalanche pairs. The likelihood is defined as the probability

$(e^{-\lambda_1}\lambda_1{}^{m_1}/m1!) \times \ldots \times (e^{-\lambda_{150}}\lambda_{150}{}^{m_{150}}/m_{150}!)$ of observing $m_1, \ldots, m_{150}$ pairs of avalanches separated by a distance $[r = 0, r + \delta r = 0.5$ mm$], \ldots, [r = 74.5$ mm, $r + \delta r = 75$ mm$]$ for a Poisson random variable of parameter $\lambda_1 = N\,P[r\in(0, 0.5$ mm$)], \ldots, \lambda_{150} = N\,P[r\in(74.5$ mm, 75 mm$)]$, where N is the total number of pairs. Occurrence by chance of the departure of $P_{\Delta n}(r)$ from $P(r)$ observed for $\Delta n = 1$ to 5 (Fig. 3, left graph) is, for example, obtained once every $e^{(-470+587)} \approx 10^{50}$ random samples. Significant departure (transient triggering at small distances) is observed for Δn ranging from 1 to about 80. Decay of $P_{\Delta n}(r) - P(r)$ with Δn follows a power law for Δn ranging from 10 to about 100.

rial with high dislocation mobility (*7*). A similar correlation analysis applied to different sets of 200 successive events did not reveal any significant evolution of D with increasing deformation. This contrasts with an increasing clustering (revealed by a decrease of D) of hypocenters during the microfracturing of rocks under creep loading (*16*) or obtained with a numerical model of brittle damage (*18*). Several hypotheses can be tentatively proposed to explain this difference, including the dimensionality of the interacting entities (1D for dislocations, 2D for cracks), the nature of their interacting stress fields (decreasing in $1/r$ for dislocations, $1/\sqrt{r}$ for cracks), or the irreversible nature of cracking (at experimental time scales) that induces a positive feedback loop favoring the localization of damage.

The emergence of this spatial clustering of dislocation avalanches (Fig. 2) may come from the dynamical interactions between avalanches, because new avalanches might be more likely to occur close to recent ones. Such a space/time coupling in the collective dislocation dynamics is investigated by means of a space/time correlation analysis. The probability distribution $P_{\Delta n}(r)$ of the distance r separating the nth and the $(n + \Delta n)$th avalanche is computed for various Δn's. The occurrence rank n rather than the occurrence time t is used here, given the strong nonstationarity of the macroscopic creep. $P_{\Delta n}(r)$ is a conditional probability; that is, the probability of two events being spatially separated by a distance r, knowing that they are separated in time by Δn events. If no significant space/time coupling is present in the dynamics, then the conditional probability $P_{\Delta n}(r)$ should be identical to the nonconditional probability $P(r)$ [the

derivative of the correlation integral $C(r)$ of Fig. 2], within the standard deviation of the numerical noise due to limited sampling. On the contrary, the difference $P_{\Delta n}(r) - P(r)$ should increase as Δn decreases if local, transient perturbation of the probability of avalanche occurrence follows any given avalanche. Such a difference is observed for small Δn's (Fig. 3). The significance of this difference is measured by a log-likelihood function based on a Poissonian representation (Fig. 4). It is significant for $\Delta n \leq 80$, after which the transient changes triggered by an avalanche are not detectable anymore. No significant modification of this spatiotemporal behavior was detected between the three directions (x, y, and z). This space/time coupling reveals that the occurrence of an avalanche increases, on average, the rate of subsequent avalanches in its vicinity during a limited time $\Delta n < \Delta n_c$, a possible mechanism for which is through stress redistribution. This limited time Δn_c might arise from limited sampling and could diverge to infinity as larger data sets are considered. One could then envisage a cascade process in which avalanches positively modulate the occurrence probability of the subsequent avalanches in their vicinity, which in turn modify the occurrence probability of the third generation of avalanches, and so on, at increasing distances (on average) from the avalanches of the first generation. This diffusion has been documented for earthquakes (*19*). Here, the mean of the distribution of $P_{\Delta n}(r) - P(r)$ is found to slowly increase with Δn. This reveals a diffusion of the avalanche interaction [a relative increase of $P_{\Delta n}(r) - P(r)$ at large r as compared to small r as Δn increases], although it is slow compared to Brownian diffusion or even to what is typically observed in fracturing and faulting at larger scales (*19*).

Dislocation avalanches are clustered in space according to scale-free patterns and are found to dynamically interact between themselves. Such observations strengthen the view that plastic flow can be associated with collective phenomena: Moving dislocations organize into avalanches that are themselves dynamically coupled into avalanche clusters.

References and Notes
1. H. Neuhauser, in *Dislocations in Solids*, F. R. N. Nabarro, Ed. (North-Holland Publishing, Amsterdam, Netherlands, 1983), pp. 319–440.
2. P. Hahner, K. Bay, M. Zaiser, *Phys. Rev. Lett.* **81**, 2470 (1998).
3. F. Szekely, I. Groma, J. Lendvai, *Mat. Sci. Eng. A* **309-310**, 352 (2001).
4. J. Gil Sevillano, E. Bouchaud, L. P. Kubin, *Scripta Met. Mat.* **25**, 355 (1991).
5. G. Ananthakrishina, S. J. Noronha, C. Fressengeas, L. P. Kubin, *Phys. Rev. E* **60**, 5455 (1999).
6. J. Weiss, F. Lahaie, J. R. Grasso, *J. Geophys. Res.* **105**, 433 (2000).
7. M. C. Miguel, A. Vespignani, S. Zapperi, J. Weiss, J. R. Grasso, *Nature* **410**, 667 (2001).
8. The interpretation of acoustic amplitudes and energies in terms of dislocation dynamics is available as supporting material on *Science* Online.
9. J. P. Sethna, K. A. Dahmen, C. R. Myers, *Nature* **410**, 242 (2001).

10. A. Petri, G. Paparo, A. Vespignani, A. Alippi, M. Costantini, *Phys. Rev. Lett.* **73**, 3423 (1994).
11. S. Zapperi, P. Ray, H. E. Stanley, A. Vespignani, *Phys. Rev. E* **59**, 5049 (1999).
12. J. Weiss, J. R. Grasso, M. C. Miguel, A. Vespignani, S. Zapperi, *Mat. Sci. Eng. A* **309-310**, 360 (2001).
13. M. Zaiser, *Mat. Sci. Eng. A* **309-310**, 304 (2001).
14. J. Weiss, J. R. Grasso, *J. Phys. Chem.* **101**, 6113 (1997).
15. P. Duval, O. Castelnau, *J. Phys. IV* **5**, C3-197 (1995).
16. T. Hirata, T. Satoh, K. Ito, *Geophys. J. R. Astron. Soc.* **90**, 369 (1987).
17. D. A. Lockner, J. D. Byerlee, V. Kuksenko, A. Ponomarev, A. Sidorin, *Nature* **350**, 39 (1991).
18. D. Amitrano, J. R. Grasso, D. Hantz, *Geophys. Res. Lett.* **26**, 2109 (1999).
19. D. Marsan, C. J. Bean, S. Steacy, J. McCloskey, *J. Geophys. Res.* **105**, 28081 (2000).
20. We thank A. Demongeot for preparation of the ice crystals, M. C. Miguel and P. Duval for interesting discussions and comments, and G. O'Brien for English corrections.

Phengite-Based Chronology of K- and Ba-Rich Fluid Flow in Two Paleosubduction Zones

E. J. Catlos[1]* and S. S. Sorensen[2]

Subduction recycles aqueous fluids from slab and sediment to the mantle. Subduction zones are long-lived, but time scales for fluid-rock interaction within subduction complexes are uncertain. Large-ion lithophile elements (potassium and barium) were added to eclogite (subducted basalt) during high pressure/temperature metamorphism via phengite crystallization from subduction zone fluids. Phengite grains from eclogite blocks and their metasomatic selvages yielded $^{40}Ar/^{39}Ar$ ages across grains and between samples that indicate 25 and 60 million years of fluid-rock interaction in the Samana Complex, Dominican Republic, and the Franciscan Complex, California, respectively.

Phengite, the principal host of large-ion lithophile elements (LILEs; here, K and Ba) in subduction zone metabasalts, carries these elements to depths of more than 180 km (*1–3*). Phengite dehydration at high pressure and temperature (*P/T*) conditions produces LILE- and H_2O-rich fluids, which can transfer these components to the overlying mantle wedge and through shallower levels of the subduction complex (*2, 4*). Large (0.2 to 4 mm) phengite grains in eclogite blocks and zoned selvages (rinds) around the blocks from two high-*P/T* metamorphic terrains (the Samana Metamorphic Complex in the Dominican Republic and the Franciscan Complex in California) contain 0.2 to 1.6 weight percent (wt %) BaO (table S1) (*5*). The Ba zoning patterns of phengite grains suggest that they formed from LILE-rich fluid-rock interaction during subduction zone metamorphism (*3, 6*). To investigate whether Ba zoning reflects time-resolvable fluid-rock events, we obtained $^{40}Ar/^{39}Ar$ ages for these grains.

The Samana Metamorphic Complex (Fig. 1) contains eclogite blocks produced during subduction of the North American plate beneath the Caribbean plate (supporting online text) (*7, 8*). Glaucophane Sm/Nd ages suggest eclogite fa-

cies metamorphism at 84 ± 22 million years ago (Ma) (*9*), and phengite K-Ar ages of 38 ± 2 Ma record retrogression and uplift due to slip along the Septentrional fault zone, the present North American–Caribbean plate boundary (*7, 8, 10*). Two blocks from Punta Balandra (SS84-24A and SS85-27E), their transition zones and inner rinds (SS84-24B, SS84-24C, and SS85-27B1), and their actinolite-rich outer rinds (SS84-24D and SS85-27B2) yielded phengite grains (Fig. 2) (*3*).

The Franciscan Complex (Fig. 1) contains garnet blueschist, garnet amphibolite, and eclogite blocks (Fig. 2) (supporting online text) (*11*). It formed during east-dipping Mesozoic subduction beneath the western margin of the North American plate and is cut by the Miocene-initiated San Andreas Fault system. Jurassic to early Tertiary K-Ar ages for Franciscan whole rocks, glaucophane, hornblende, and white mica (*12–17*) may reflect eclogite or amphibolite facies metamorphism at 163 to 158 Ma, cooling to below phengite's Ar closure *T* between 159 and 139 Ma, and continuing blueschist *P/T* conditions from ~146 to 80 Ma (*17*).

Franciscan Complex samples analyzed here are from Ring Mountain in the Tiburon Peninsula (*12, 18*) and Mount Hamilton in the Diablo Range (*3, 13, 19–21*). Tiburon samples include garnet amphibolite (T-90-2AH) and eclogite blocks (T-90-3AG and T-90-3AB), actinolite-rich rind (T-90-2B), and cross-cutting phengite and a chlorite vein (T-90-2V). Mount Hamilton samples include an eclogite block (MH-90-1AB), a garnet amphibolite layer within the

[1]School of Geology, Oklahoma State University, 105 Noble Research Center, Stillwater, OK 74078, USA. [2]Department of Mineral Sciences, NHB-119, National Museum of Natural History, Smithsonian Institution, Washington, DC 20560–0119, USA.

*To whom correspondence should be addressed. E-mail: catlos@okstate.edu

Table 1. Samana $^{40}Ar/^{39}Ar$ phengite ages, with ±1σ uncertainties. The 48 Samana analyses together average 37.8 ± 2.6 My, with a MSWD of 13. See Fig. 2 for average ages and MSWD for each sample. For each sample, numbers in parentheses indicate the grain and spot number, respectively.

Sample	Age (My)
Eclogite blocks	
SS84-24A (2-3)	25.5 ± 2.5
SS84-24A (2-2)	29.8 ± 3.0
SS84-24A (2-1)	30.6 ± 1.1
SS84-24A (1-1)	31.0 ± 4.7
SS84-24A (1-3)	31.2 ± 1.7
SS84-24A (1-2)	31.6 ± 1.9
SS84-24A (1-4)	32.1 ± 2.4
SS85-27E (2-1)	29.2 ± 1.3
SS85-27E (1-1)	31.8 ± 4.3
SS85-27E (3-1)	32.1 ± 1.7
SS85-27E (2-2)	32.4 ± 1.5
SS85-27E (3-2)	35.8 ± 2.6
Inner rinds	
SS84-24B (1-1)	39.5 ± 1.2
SS84-24B (1-2)	42.2 ± 0.7
SS84-24B (2-2)	43.5 ± 1.2
SS84-24B (1-3)	45.2 ± 0.4
SS84-24B (2-3)	45.7 ± 2.5
SS84-24B (2-1)	46.1 ± 2.0
SS85-27B1 (2-4)	42.5 ± 1.8
SS85-27B1 (3-1)	43.6 ± 1.7
SS85-27B1 (2-3)	45.5 ± 1.8
SS85-27B1 (2-2)	48.9 ± 3.7
Transition zone and outer rinds	
SS84-24C (1-4)	34.8 ± 1.2
SS84-24C (2-1)	37.5 ± 1.5
SS84-24C (1-3)	39.0 ± 0.8
SS84-24C (1-2)	39.1 ± 1.2
SS84-24C (1-1)	40.8 ± 0.5
SS84-24C (2-2)	44.9 ± 0.7
SS85-27B2 (1-2)	24.7 ± 3.7
SS85-27B2 (1-3)	31.9 ± 3.3
SS85-27B2 (1-1)	32.7 ± 1.1
SS85-27B2 (3-2)	36.7 ± 4.9
SS85-27B2 (2-1)	40.2 ± 1.1
SS85-27B2 (3-1)	43.2 ± 4.2
SS85-27B2 (3-3)	43.5 ± 3.9
SS85-27B2 (2-2)	46.1 ± 1.3
SS84-24D (1-1)	33.7 ± 5.2
SS84-24D (1-8)	36.2 ± 2.8
SS84-24D (1-6)	36.7 ± 2.1
SS84-24D (1-2)	37.4 ± 5.4
SS84-24D (1-10)	37.5 ± 1.5
SS84-24D (1-4)	37.7 ± 1.2
SS84-24D (1-3)	38.0 ± 2.2
SS84-24D (1-9)	39.4 ± 1.5
SS84-24D (2-1)	39.5 ± 2.8
SS84-24D (1-5)	39.8 ± 1.1
SS84-24D (1-7)	40.8 ± 0.8
SS84-24D (1-11)	44.7 ± 3.5

Science

Three-Dimensional Mapping of Dislocation Avalanches: Clustering and Space/Time Coupling

Jérôme Weiss and David Marsan

ARTICLE TOOLS	http://science.sciencemag.org/content/299/5603/89
SUPPLEMENTARY MATERIALS	http://science.sciencemag.org/content/suppl/2003/01/02/299.5603.89.DC1
REFERENCES	This article cites 16 articles, 0 of which you can access for free http://science.sciencemag.org/content/299/5603/89#BIBL
PERMISSIONS	http://www.sciencemag.org/help/reprints-and-permissions

Use of this article is subject to the Terms of Service